EUROPEAN ORGANIZATION FOR NUCLEAR RESEARCH

CERN Summer Student Programme 2025
Project Report
October 6, 2025

Measurement of Σ hyperons using the upgraded ALICE ITS

Matteo Morgante[1,2]

Supervisors: Francesco Mazzaschi[1] and Maximiliano Puccio[1]

1. European Organization for Nuclear Research (CERN)
2. Università di Padova

Abstract

In this work, the measurement of Σ^- and Σ^+ production in minimum-bias pp collisions at $\sqrt{s}$ = 13.6 TeV is presented. Charged Σ hyperons are reconstructed with a novel approach, directly analyzing the kink topology of their main decay branches, which all include a neutral daughter in the final state. The reconstruction efficiency of this method for each decay channel is studied. The p_{T}-differential spectra and the integrated yields of both Σ^- and Σ^+ are reported and compared with the ones obtained from Run 2 pp collisions at $\sqrt{s}$ = 13 TeV. An additional cross-check on Ξ^- production is also presented, to better analyze possible causes of discrepancy between the results of Run 3 and Run 2.

1 Introduction and physics motivation

Σ hyperons are the members of the isospin triplet with $S = -1$ in the $J^{\pi} = \frac{1}{2}^{+}$ SU(3) baryon octet. Unlike many other particles, measurements of their production in hadronic or heavy-ion collisions are rarely found in the literature. This is because none of these baryons has a purely charged decay channel: there is always at least a neutral particle in the final state and, as a consequence, techniques that rely on the detection of all daughters cannot be used effectively to reconstruct the decay kinematics.

Such limitation can now be overcome with the upgraded Inner Tracking System (ITS) installed by ALICE for LHC Run 3 [1, 2, 3]. The ITS features 12 billion silicon pixels arranged in seven layers, with the innermost three located within 4 cm of the interaction point. Charged particles crossing the detector leave signals that allow the reconstruction of their trajectories with a spatial precision of about 5 μm. These features allow the tracking of short-lived primary particles such as Σ hyperons, as they are characterized by a $c\tau \sim 5$ cm [4]. Combining the information on the mother track with the partial ones on the final state, the kinematics of their decays into a neutral daughter can be deduced in a complete way.

The development of an analysis method that allows the selection and reconstruction of Σ baryons with high efficiency and signal purity enables plenty of applications with physical relevance, such as:

- studies of the strangeness enhancement phenomenon in the Σ sector;
- precise measurements of poorly understood resonance states that decay into a Σ daughter, such as the $\Lambda(1405)$. The $\Lambda(1405)$ is a key state to investigate the $\bar{K}N$ interaction and the possible existence of molecular-like configurations [5];
- studies of the interactions of Σ baryons with protons in the context of femtoscopic measurements. Measuring the Σ-p correlation function could be crucial for a better understanding of the equation of state of neutron stars, an important piece for the solution of the baryon cocktail puzzle for the composition of these astrophysical systems [6].

In this report, measurements of the production yield of Σ^- and Σ^+ hyperons in pp collisions at $\sqrt{s}$ = 13.6 TeV are presented; in particular, the p_{T}-differential yield of Σ^- is computed for the first time. These measurements are carried out thanks to a new technique based on the direct reconstruction of the kink topology of the main decay channels of these baryons, $\Sigma^{\pm} \rightarrow \mathrm{n} + \pi^{\pm}$ and $\Sigma^{+} \rightarrow \mathrm{p} + \pi^{0}$.

2 Analysis framework

The analysis shown in this report is performed in O2Physics and is mainly based on the kink builder task (kinkBuilder.cxx) for decay reconstruction, and on the sigma minus task (sigmaminustask.cxx) for the post-processing of kink candidates. The kink builder task reconstructs the topology of two body decays which involve a neutral particle in the final state by matching a mother track, selected as an ITS only track with at least 4 hits in the 4 layers that are closer to the collision point, with a charged daughter track, chosen among tracks with hits detected in both the ITS and the TPC. If the two tracks are compatible and close to each other, a DCA fitter is used to reconstruct the secondary vertex of the decay. The relevant information about each kink decay candidate found in this way is then passed to the sigma minus task, where further topological and kinematic selections are applied to isolate the decay channels of interest. Finally, the data are stored in histograms and tables for further post-processing steps.

3 Data sample and selection criteria

The data set analyzed in this work was recorded in 2024 during the LHC pp run at $\sqrt{s}$ = 13.6 TeV and consists of $1.01 \cdot 10^{10}$ selected triggered events. A general purpose Monte Carlo data sample, anchored to the 2024 data, was used for the computation of the efficiency corrections and to perform the closure test on the signal extraction procedure. This sample consists of $1.4 \cdot 10^{9}$ selected generated pp collisions.

Several selection criteria are applied to ensure track quality, reconstruction accuracy, and finally to achieve good purity levels for the final signal distributions. At the kink builder level and in general for all decay channels analyzed, the most relevant cuts are the following:

- z coordinate of the primary vertex is required to be within 10 cm from the collision point, to guarantee uniformity in the detector acceptance;
- the daughter track needs to have at least 80 clusters in the TPC;
- the pseudorapidity range for mother tracks is $|\eta| < 1.0$, while for charged daughter ones is $|\eta| < 0.8$, to ensure they stay within the acceptance of the ITS;
- the distance of closest approach (DCA) to the primary vertex for mother tracks is required to be smaller than 0.25 mm, for daughter tracks it has to be greater than 1 mm;
- the pointing angle (PA) of the decay candidate, defined as

$$\mathrm{PA} = \arccos\left(\frac{\vec{r}\cdot\vec{p}_{\mathrm{moth}}}{|\vec{r}|\cdot|\vec{p}_{\mathrm{moth}}|}\right) \tag{1}$$

  where $\vec{r}$ is the decay vertex position with respect to the primary vertex and $\vec{p}_{\mathrm{moth}}$ is the mother momentum vector, needs to be smaller than 5^{o};

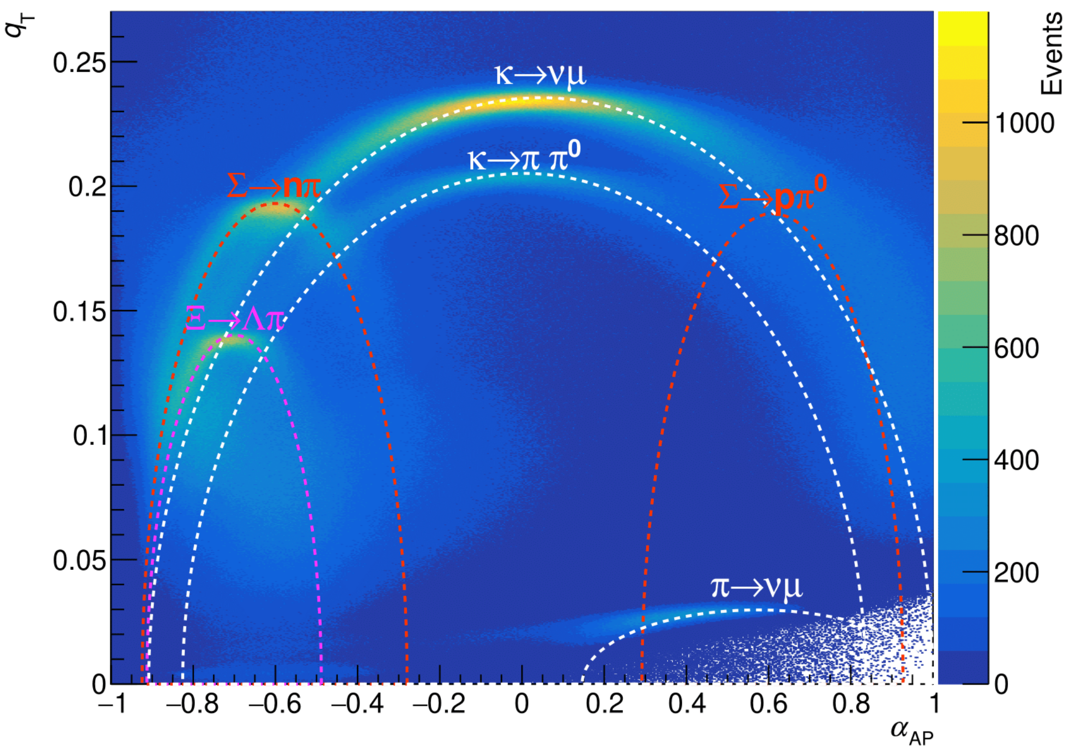

Fig. 1: Armenteros-Podolanski plot of all reconstructed kink topology decays. Highlighted the half-ellipse curves along which different decay topologies should lie.

Additional selections are applied to separate the signals for the decay channels of interest. In this analysis Σ baryons are identified by studying their main decay branches that are [4]:

$$\Sigma^- \to \mathrm{n}+\pi^- \qquad (\overline{\Sigma}^+ \to \overline{\mathrm{n}}+\pi^+) \qquad \mathrm{B.R.} = (99.848\pm0.005)\% \tag{2}$$

$$\Sigma^+ \to \mathrm{n}+\pi^+ \qquad (\overline{\Sigma}^- \to \overline{\mathrm{n}}+\pi^-) \qquad \mathrm{B.R.} = (48.4\pm0.3)\% \tag{3}$$

$$\Sigma^+ \to \mathrm{p}+\pi^0 \qquad (\overline{\Sigma}^- \to \overline{\mathrm{p}}+\pi^0) \qquad \mathrm{B.R.} = (51.5\pm0.3)\% \tag{4}$$

To isolate these topologies from other reconstructed kink candidates, we used:

- Particle identification cuts on charged daughter tracks. The specific energy loss $\mathrm{d}E/\mathrm{d}x$ in the TPC gas was required to be within 4σ of its expected value for both π and p daughters. In addition to this, a 5σ selection is implemented on the Time-of-Flight signal specifically for p daughters, to significantly enhance the purity of the channel.
- Topologically specific cuts on the Armenteros-Podolanski variables $(\alpha^{\mathrm{AP}}, q_{\mathrm{T}}^{\mathrm{AP}})$ [7] defined as follows

$$\alpha^{\mathrm{AP}} = \frac{p_{\mathrm{L}}^{\mathrm{ch}} - p_{\mathrm{L}}^{\mathrm{neut}}}{p_{\mathrm{L}}^{\mathrm{ch}} + p_{\mathrm{L}}^{\mathrm{neut}}}, \qquad q_{\mathrm{T}}^{\mathrm{AP}} = \frac{|\vec{p}_{\mathrm{ch}}|^2 - |\vec{p}_{\mathrm{ch}} \cdot \vec{p}_{\mathrm{moth}}|^2}{|\vec{p}_{\mathrm{moth}}|^2}. \tag{5}$$

  where $\vec{p}_{\mathrm{moth}}$ is the mother momentum, $\vec{p}_{\mathrm{ch}}$ the charged daughter momentum, $\vec{p}_{\mathrm{neut}} = \vec{p}_{\mathrm{moth}} - \vec{p}_{\mathrm{ch}}$ the neutral daughter momentum and p_{L} refers to the longitudinal projection of $\vec{p}$ on the mother momentum. After analyzing the Armenteros-Podolanski plot (Fig. 1) and having computed the expected curves along which the events referring to the decays of interest lie, the region selected to isolate the Σ baryons is determined by $0.15 < q_{\mathrm{T}}^{\mathrm{AP}} < 0.20$, with $\alpha^{\mathrm{AP}} < 0$ for decays into $\mathrm{n} + \pi^{\pm}$, and $\alpha^{\mathrm{AP}} > 0$ for the $\mathrm{p} + \pi^0$ branch.

4 Efficiency × acceptance

The first analysis step after the selection criteria definition is a detailed study of the efficiency of reconstruction and the acceptance of the detector, quantities that are obtained using the MC generated sample connected to the data. The definition of efficiency × acceptance as a function of p_{T} is:

$$\varepsilon(\Delta p_{\mathrm{T}}) = \frac{N_{\mathrm{rec}}(\Delta p_{\mathrm{T}})}{N_{\mathrm{gen}}(\Delta p_{\mathrm{T}})} \tag{6}$$

where N_{rec} is the number of MC particles correctly reconstructed by applying the same selection criteria used for the experimental data, while N_{gen} is the total number of MC generated particles. An efficiency × acceptance curve is computed for each particle and decay channel analyzed: each time in N_{rec}, N_{gen} only MC-truth verified events that belong to such channel are included in the count. The efficiency values with respect to different p_{T} intervals are shown in Fig. 2-(left panel): the dependence on p_{T} is strong, with a decrease towards lower transverse momenta. This happens because the lower the p_{T} , the lower the probability that a Σ decays after the 4^{th} ITS layer and hence is reconstructed. It can also be noticed that the reconstruction efficiency for Σ^+ is significantly lower, in both channels, compared to the Σ^- one.

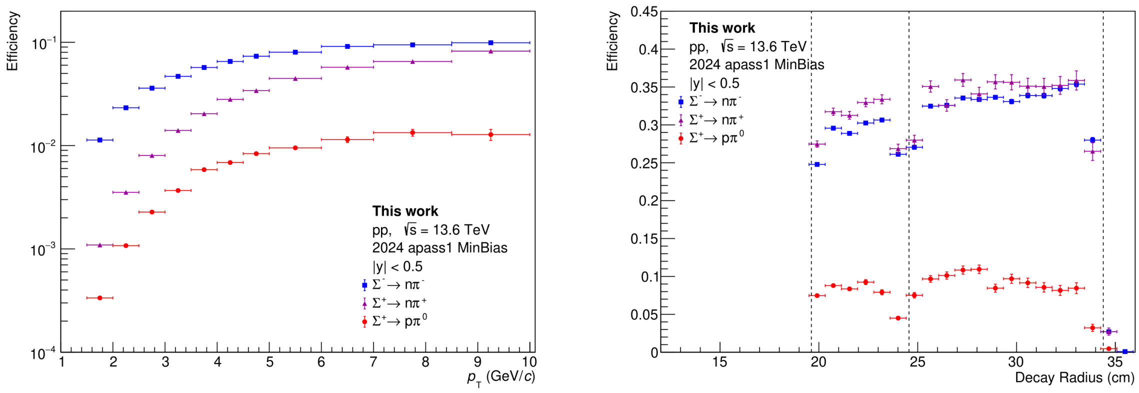

Fig. 2: Efficiency as a function of the transverse momentum (left) and of the reconstructed decay radius (right) of the three decay channels analyzed. In the right panel, the positions of the $4^{\mathrm{th}}, 5^{\mathrm{th}}$ and 6^{th} ITS layers are shown as vertical dashed lines. Error bars of the data points correspond to the statistical uncertainties.

To better investigate the sources of efficiency loss for Σ^+, the ratios between the efficiencies obtained for Σ^+ and Σ^- were compared with the expected Σ^+/Σ^- ratio for particles decaying in the active range $r \in [19.6, 34.4]$ cm, calculated assuming equal production at the collision point. The Σ^+/Σ^- ratio was obtained with the following expression, which estimates the decay probability ratio for the two particles within the range of interest:

$$\frac{N(\Sigma^+)}{N(\Sigma^-)}(p_{\mathrm{T}}) = \frac{P_+(p_{\mathrm{T}}; r_{\mathrm{min}}) - P_+(p_{\mathrm{T}}; r_{\mathrm{max}})}{P_-(p_{\mathrm{T}}; r_{\mathrm{min}}) - P_-(p_{\mathrm{T}}; r_{\mathrm{max}})}, \qquad P_\pm(p_{\mathrm{T}}; r) = \exp\left(-\frac{r m_\pm}{c\tau_\pm p_{\mathrm{T}}}\right) \tag{7}$$

The results are reported in Fig. 3: the dashed black line represents the prediction derived from equation 7, which is perfectly compatible with the ratio computed from the generated Σs in the MC simulation, in green. For what regards the $\Sigma^+ \rightarrow \mathrm{n} + \pi^+$ channel, the Σ^+ to Σ^- efficiency ratio follows the expectations at low p_{T}, with a $\approx 10\%$ minor discrepancy arising when transverse momentum increases. For this channel, the difference in efficiency between Σ^+ and Σ^- is then explained by the lifetime difference between the two particles. Instead, a major loss is observed for the $\Sigma^+ \rightarrow \mathrm{p} + \pi^0$ branch: in this case, to get a better insight, the efficiency ratio obatined without requesting a TOF signal for the proton daughter has also been plotted, in magenta, to compare it with the actual ratio computed including this selection, in blue. This comparison highlights two sources of efficiency loss for the channel:

- the TOF selection introduces a ≈ 4 efficiency reduction, approximately constant in p_{T} ;
- the decay kinematics produce an additional factor, which is negligible at low p_{T} and increases up to ≈ 2 at 10 GeV/c. This is due to the small mass difference between the Σ^+ and the proton daughter, which implies a lower kink decay angle, especially at higher p_{T}. If the decay angle is very small, it becomes more difficult for the detector to resolve and distinguish between the tracks of mother and daughter, which may become merged in a single track with higher probability.

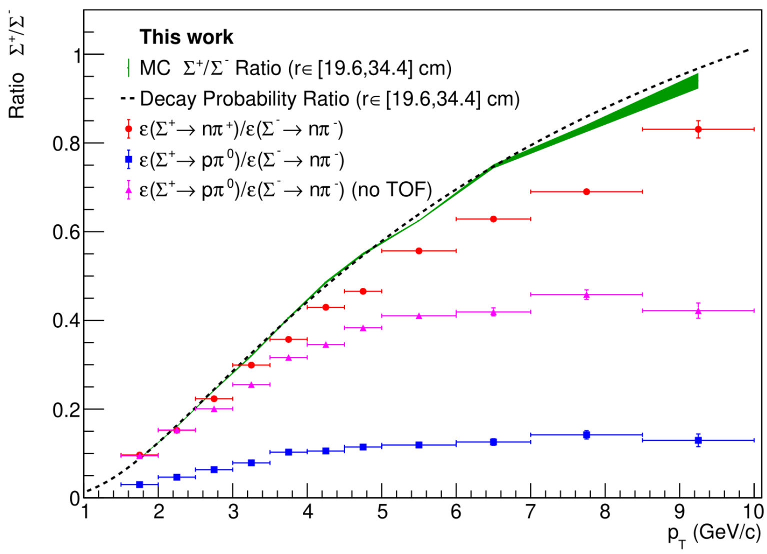

Fig. 3: Comparison between the expected Σ^+/Σ^- ratio for particles decaying in the range $r \in [19.6, 34.4]$ cm and the efficiency ratio of Σ^+ and Σ^- for different decay channels.

The efficiency behavior with respect to the decay radius of the Σ mother is also reported, in the right panel of Fig. 2. The radius dependence of efficiency is basically constant within the active selection region of the kink builder algorithm, located between the 4^{th} and the 6^{th} ITS layer. The efficiencies of Σ^+ and Σ^- in the n+$\pi^\pm$ channel are comparable; there is a ≈ 3.5 loss factor for the p +π^0 channel, mainly due to the additional TOF selection needed for the identification of the proton daughter.

4.1 p_{T} and decay radius resolution

The resolution in both reconstructed transverse momentum and decay radius was also studied. The relative difference δ between reconstructed p_{T} (r) and the MC-truth quantity was computed for each Σ generated, tagged and correctly reconstructed in the MC sample.

$$\delta_{p_{\mathrm{T}}}(p_{\mathrm{T}}) = \frac{p_{\mathrm{T}}^{\mathrm{rec}} - p_{\mathrm{T}}^{\mathrm{gen}}}{p_{\mathrm{T}}^{\mathrm{gen}}} \qquad \delta_r(r) = \frac{r^{\mathrm{rec}} - r^{\mathrm{gen}}}{r^{\mathrm{gen}}} \tag{8}$$

The δ distributions were later analyzed, extracting their average width with a Gaussian fit for each p_{T} (r) interval to obtain the resolution trend. The results of this analysis are shown in Fig. 4. The relative resolution in p_{T} is of 9% at 2 GeV/c and increases approximately linearly with momentum, reaching 14% at 6 GeV/c. The spatial resolution in decay radius is instead of the order of 0.1-0.2% and exhibits a clear systematic trend with a discontinuity in correspondence of the 5$^{\mathrm{th}}$ ITS layer position. Such artifact is probably introduced by the DCA fitter used by the kink builder to reconstruct secondary vertices.

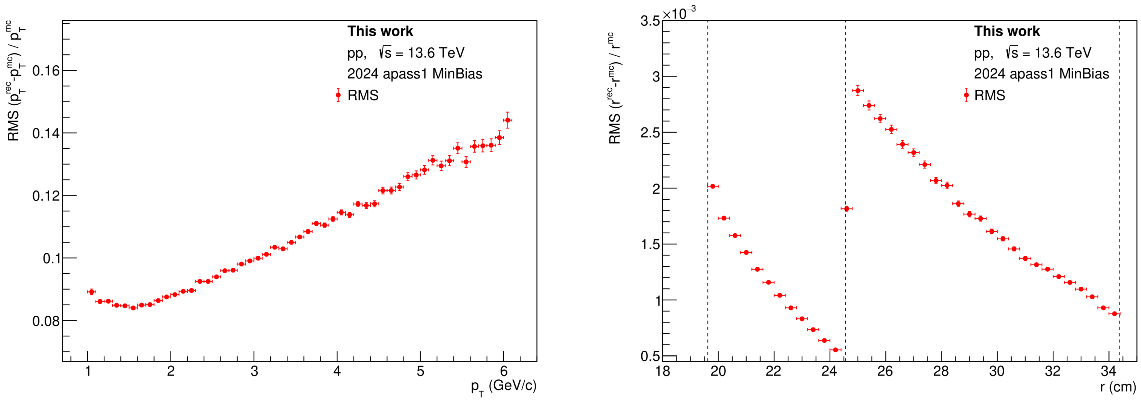

Fig. 4: Relative resolution in transverse momentum (left) and decay radius (right). In the right panel, the positions of the 4$^{\mathrm{th}}$, 5$^{\mathrm{th}}$ and 6$^{\mathrm{th}}$ ITS layers are shown as vertical dashed lines. Error bars of the data points correspond to the statistical uncertainties.

5 Signal extraction

Once all selection cuts are applied, the invariant mass distributions are fitted in order to extract the raw spectra. The fit functions used are different for the two decay channels analyzed, as in (n + $\pi^{\pm}$) distributions, both Σ^+ and Σ^- components are present, while only Σ^+ appear in the (p + π^0) channel. To build the combinatorial background, in both cases a rotational technique was used. The entire pool of kink candidates that passed the common selections was considered: for all candidates, the daughters' η was shifted by several values between $\Delta\eta \in [-0.4, 0.4]$ with a minimum step of $|\Delta\eta| = 0.1$, ensuring that they remained within the acceptance range of $|\eta| < 0.8$. For each rotation, the daughters' momentum and all related kinematic variables are then calculated again. Finally, the topologically specific cuts on the Armenteros-Podolanski variables that were implemented on experimental data, are applied on this new pool of rotated decays to get the combinatorial background template for the fits.

5.1 Decay into p + π^0

The only contribution to this channel is given by the Σ^+ (and its antiparticle $\overline{\Sigma}^-$. The signal is modeled using a double-sided Crystal Ball distribution [8]. The tail parameters of the Crystal Ball $(\alpha_{\mathrm{L}}, \alpha_{\mathrm{R}}, n_{\mathrm{L}}, n_{\mathrm{R}})$ and its width σ are first obtained from a preliminary fit on the MC invariant mass distribution, obtained selecting only $\Sigma^+ \to \mathrm{p} + \pi^0$ decays. Then, for the actual fit on experimental data, such parameters are kept fixed and the Crystal Ball shape is summed to the rotational background template and convoluted with a Gaussian distribution with variable width σ_{conv}, to keep track of possible resolution differences with the MC. Some of the fitted mass distributions are shown in Fig. 5: overall the nominal mass of the Σ^+ of 1.189 GeV/c^2 [4] is compatible with the peak positions. The number of signal counts in each p_{T} bin is determined using the normalization parameter of the Crystal Ball distribution in the fit over the entire [1.15,1.33] GeV/c^2 interval, to account for all the events in the large right tail that characterizes the shape.

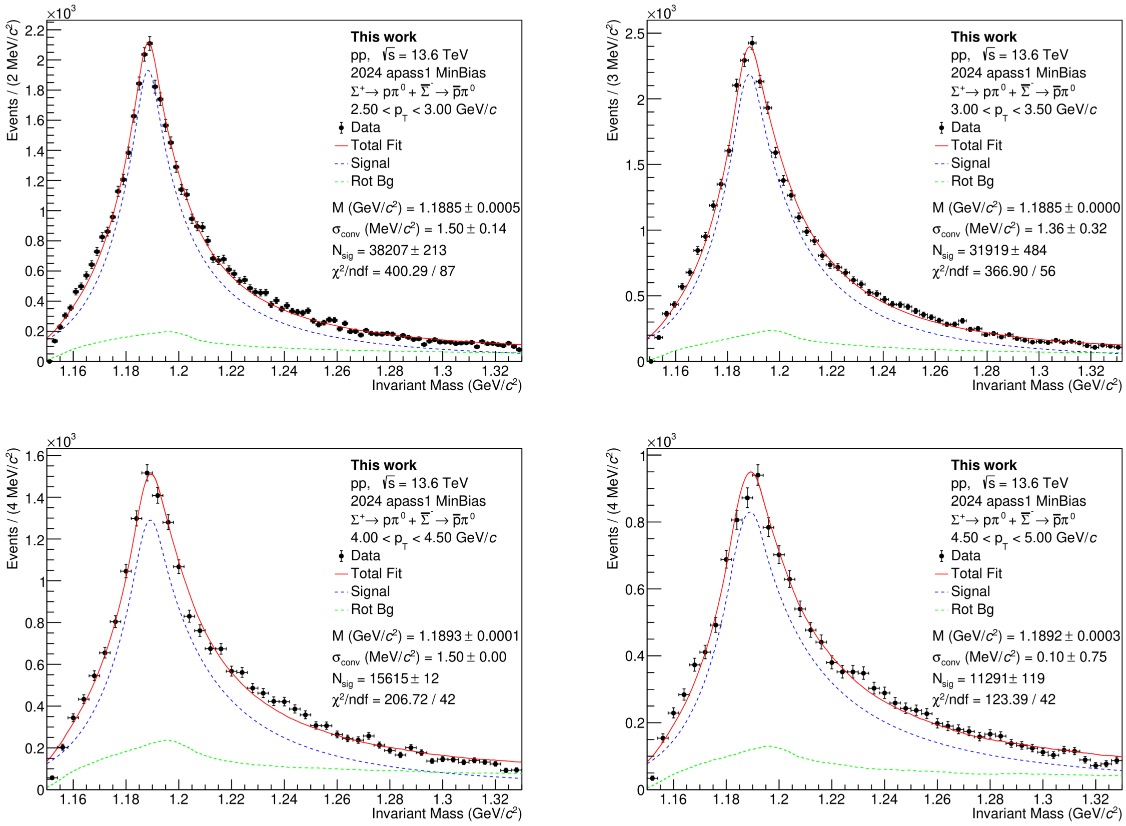

Fig. 5: Invariant-mass distributions of $\Sigma^+ + \overline{\Sigma}^-$ for the $\text{p}(\overline{\text{p}}) + \pi^0$ decay in different p_{T} intervals, as indicated in the legends. Error bars of the data points correspond to the statistical uncertainties. The total fit function is shown in red, the Crystal Ball for the signal is the dashed blue line, while the rotational background template is the dashed green curve.

5.2 Decay into n + $\pi^\pm$

The fitting procedure is similar to the previous case, although now the main peak receives contributions from both Σ^+ and Σ^-. For this reason, two different Crystal Ball curves are used to model the signal, one for each particle. The tail parameters and the width of each curve are extracted from preliminary fits on the respective MC distribution and then fixed in the main fit. The difference between the peaks' mean values is also kept fixed to the nominal mass difference between Σ^- and Σ^+ , that is $\Delta m = m_{\Sigma^-} - m_{\Sigma^+} = (8.08 \pm 0.08)$ MeV/c^2 [4]. In addition, the same Gaussian convolution factor is applied to the two Crystal Balls, again to consider resolution losses between data and MC. Fits of the two peaks over the rotational background template for some p_{T} intervals are reported in Fig. 6: the number of counts for the raw spectra extraction is computed again using the normalization factor for each Crystal Ball, evaluated over the [1.16,1.28] GeV/c^2 interval in this case.

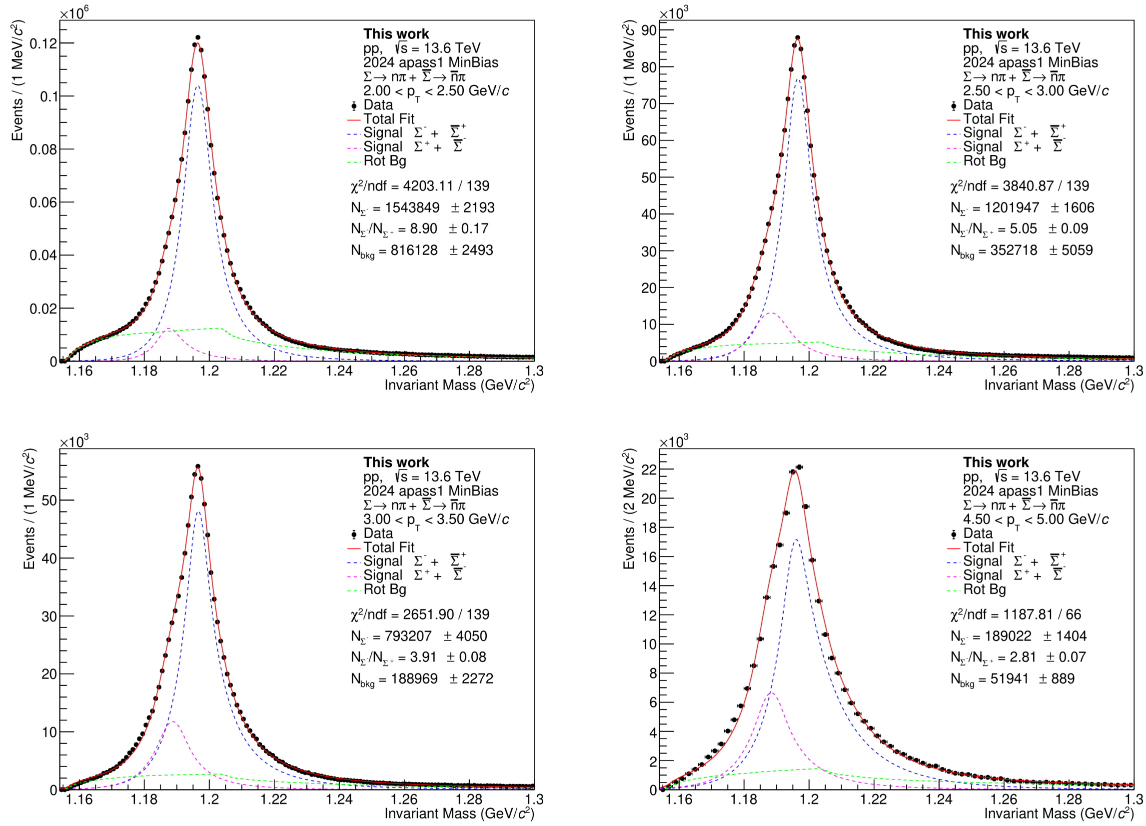

Fig. 6: Invariant-mass distributions of $\Sigma^{\pm}+\overline{\Sigma}^{\mp}$ for the $\mathrm{n}(\overline{n})+\pi^{\pm}$ decay in different p_{T} intervals. Error bars of the data points correspond to the statistical uncertainties. The Crystal Ball functions are shown respectively in blue, for the Σ^- peak, and magenta, for the Σ^+ one. The rotational background template is the dashed green line, while the total fit function, sum of all component, is in red.

6 MC closure test

To check whether the procedure used to get raw count spectra is sufficiently reliable and yields correct results, a MC closure test was performed. For such a test, the MC sample is treated as experimental data up to the signal extraction step: the same selection cuts are applied to get invariant mass distributions for both decay channels analyzed, and the same fitting procedure is followed to obtain the reconstructed estimate for the number of raw counts in each p_{T} interval. Then, the raw spectra obtained in this way are compared with the MC truth, that is, the total number of generated events that passes all selection cuts and hence should be observed in the distributions.

Some invariant mass fits on the MC sample treated as data are shown in Fig. 7. The fitting procedure for both decay channels is the one explained in the previous section, except in this case no Gaussian convolution is applied to Crystal Ball signal distributions.

Results of the closure test are reported in Fig. 8. As it can be seen, for both $\Sigma^- \to \mathrm{n}+\pi^-$ and $\Sigma^+ \to \mathrm{p}+\pi^0$ channels, the signal appears to be slightly underestimated overall, with a relative discrepancy factor within $\approx 10\%$ for all p_{T} intervals. However, the reconstructed to generated ratios are compatible with 1 within statistical uncertainties across the entire p_{T} range, with the exception of a few outliers. The closure does not work properly for the $\Sigma^+ \to \mathrm{n}+\pi^+$ channel, that is, for the signal obtained from the secondary Crystal Ball peak in the $\mathrm{n}+\pi^{\pm}$ mass distributions, which appears to be largely overestimated ($> 10\%$ discrepancy) in most fits. This implies that there is no sufficient sensitivity to correctly distinguish the actual contribution to such peak with the procedure used. In the following sections, only data

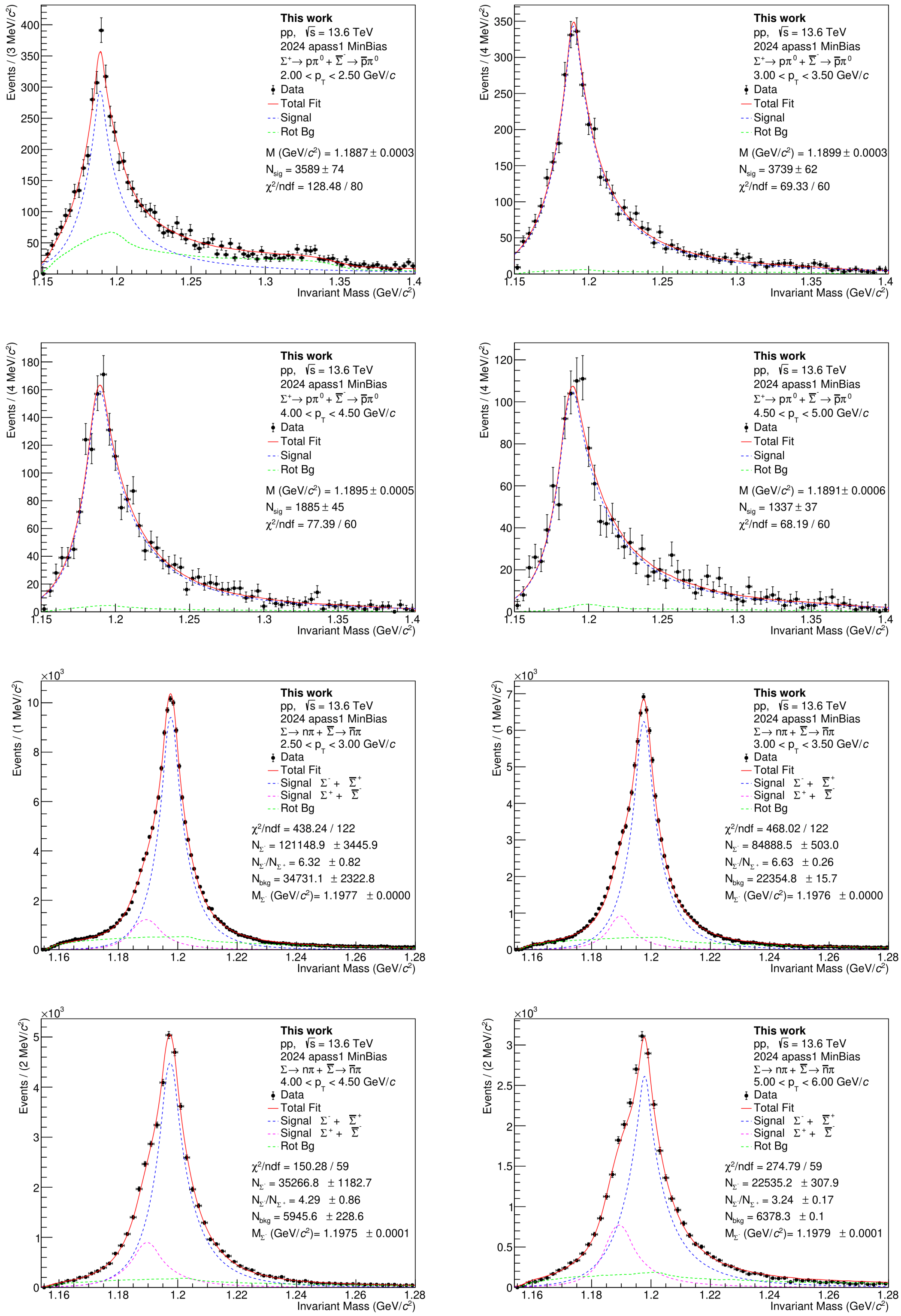

Fig. 7: Invariant-mass distributions of $\Sigma^+ + \overline{\Sigma}^-$ for the $\mathrm{p}(\overline{p}) + \pi^0$ decay (top two rows) and of $\Sigma^\pm + \overline{\Sigma}^\mp$ for the $\mathrm{n}(\overline{n}) + \pi^\pm$ decay (bottom two rows) in different p_T intervals, as indicated in the legends. Error bars of the data points correspond to the statistical uncertainties. The total fit function is shown in red, the Crystal Balls for the signal in blue (and magenta), the rotational background template in green.

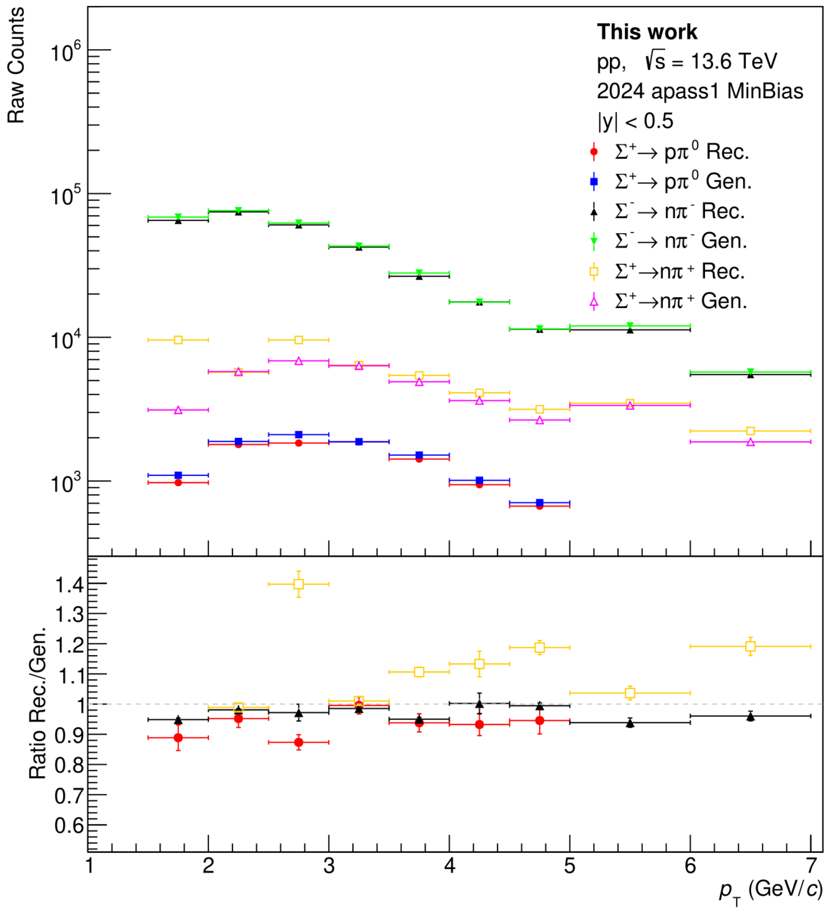

Fig. 8: MC closure of the signal extraction procedure. Comparison between the reconstructed raw spectra and the MC truth generated events that passed all selection cuts.

obtained from the two channels with successful closure results are used to compute production yields for Σ baryons.

7 Spectra computation

In this section, raw spectra obtained for $\Sigma^{\pm}$ are normalized to the total number of analyzed events and corrected with the efficiency factors necessary to extract the p_{T} differential production yields. The corrected and normalized spectra were obtained with the following expression:

$$Y_{\mathrm{corr.}}(\Delta p_{\mathrm{T}}) = \frac{1}{N^{\mathrm{true}}_{\mathrm{tot.events}}} \frac{\mathrm{d}^2 N}{\mathrm{d}p_{\mathrm{T}}\mathrm{d}y} = \frac{S_{\mathrm{raw}}(\Delta p_{\mathrm{T}})}{N^{\mathrm{obs}}_{\mathrm{tot.events}}} \cdot \frac{\varepsilon_{\mathrm{event\ loss}}}{\varepsilon_{\mathrm{eff.\times acc.}}(\Delta p_{\mathrm{T}})} \cdot \frac{1}{\Delta p_{\mathrm{T}}} \cdot \frac{1}{\Delta y} \tag{9}$$

where $S_{\mathrm{raw}}(\Delta p_{\mathrm{T}})$ are the raw counts from invariant mass fits, $N^{\mathrm{obs}}_{\mathrm{tot.events}}$ is the total number of events analyzed, $\varepsilon_{\mathrm{event\ loss}} = 0.70$ is the event loss correction to the $N^{\mathrm{obs}}_{\mathrm{tot.events}}$ factor, and finally $\varepsilon_{\mathrm{eff.\times acc.}}(\Delta p_{\mathrm{T}})$ is the efficiency × acceptance correction obtained in section 4.

The resulting normalized differential yields are shown in Fig. 9. There is great compatibility for all p_{T} intervals in the [1.5, 5.0] GeV/c^2 range between the yields of Σ^+ and Σ^- . The spectral shapes are well described by fits with Lévy-Tsallis functions [9], which are also shown in Fig. 9. From such fits, the p_{T} integrated yields $\langle \mathrm{d}N/\mathrm{d}y \rangle$ are extrapolated for both particles and reported in table 1.

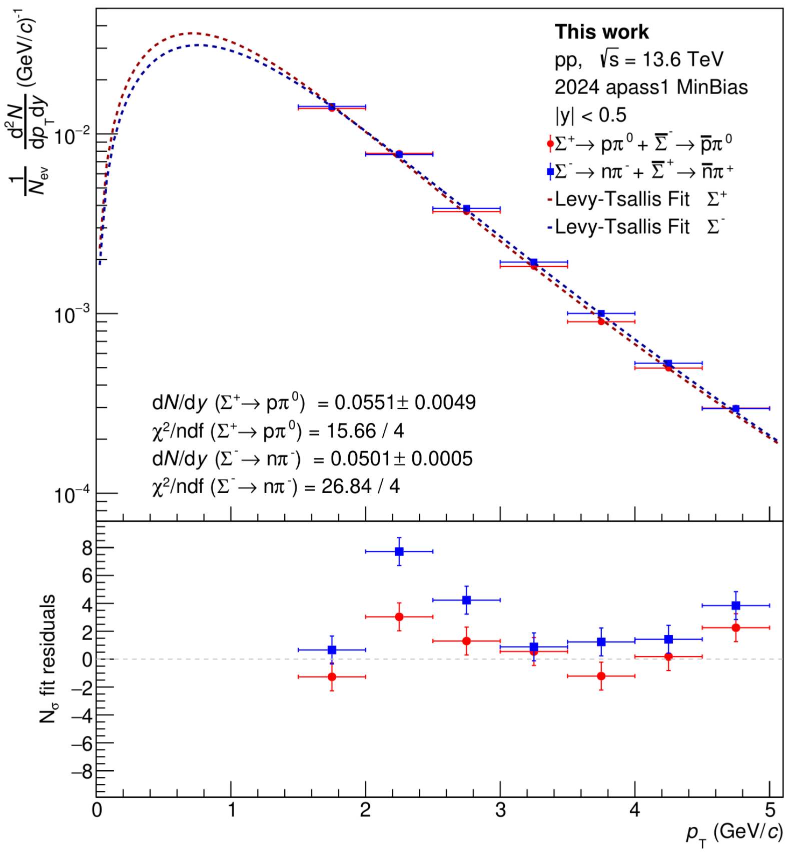

Fig. 9: Corrected and normalized p_{T}-differential yields for $\Sigma^+ + \overline{\Sigma}^-$ (red) and $\Sigma^- + \overline{\Sigma}^+$ (blue). Error bars show statistical uncertainties on the data point. The yields are fitted with Lévy-Tsallis functions [9]. In the bottom panel, normalized residuals to the fit function ($\mathrm{res} = (Y(\Delta p_{\mathrm{T}}) - f_{\mathrm{Levy}}(\Delta p_{\mathrm{T}}))/\sigma_Y$) are shown.

Particle	$\langle \frac{\mathrm{d}N}{\mathrm{d}y} \rangle$
$\Sigma^+ + \overline{\Sigma}^-$	0.055 ± 0.005 (stat)
$\Sigma^- + \overline{\Sigma}^+$	0.0501 ± 0.0005 (stat)

Table 1: p_{T} integrated yields in minimum-bias pp collisions at $\sqrt{s}$ = 13.6 TeV

7.1 Comparison with Run 2 results

The fully corrected differential yields are finally compared with the results obtained in Run 2, recently published in [11]. In that work, the production yield of Σ^+ baryons in high multiplicity and minimum-bias triggered pp collisions at $\sqrt{s}$ = 13 TeV was measured. The analysis was carried out through the reconstruction of the $\Sigma^+ \to \mathrm{p} + \pi^0$ ($\pi^0 \to \gamma + \gamma$) decay channel, where one of the photons is measured directly in the calorimeter and the other is reconstructed through the conversion to $\mathrm{e}^+ + \mathrm{e}^-$. The comparison is shown in the left panel of Fig. 10: Run 2 yield values are significantly larger than the ones obtained from Run 3 data. In particular, there is a systematic offset of 60% that is approximately constant throughout the analyzed p_{T} range.

As a first attempt to gain more insight into the discrepancies between Run 2 and Run 3 data, yields obtained from MC PYTHIA 8 simulation [10] were also calculated and compared with the results of Run 2. This comparison is shown in the right panel of Fig. 10, where in addition to the Run 2 data, the

MC generated yields computed with the reconstruction method of [11] while using the same PYTHIA 8 generator are reported. Run 2 yields are systematically higher than the ones predicted by the MC generator: the ratio between Run 2 data and MC yield is approximately equal to 2 and constant across the p_{T} range. However, when PYTHIA 8 generated yields computed with the techniques illustrated in this work are compared with the ones obtained from the same generator, but using the methods of Run 2, the compatibility is great: MC results appear to be independent of the extraction method applied.

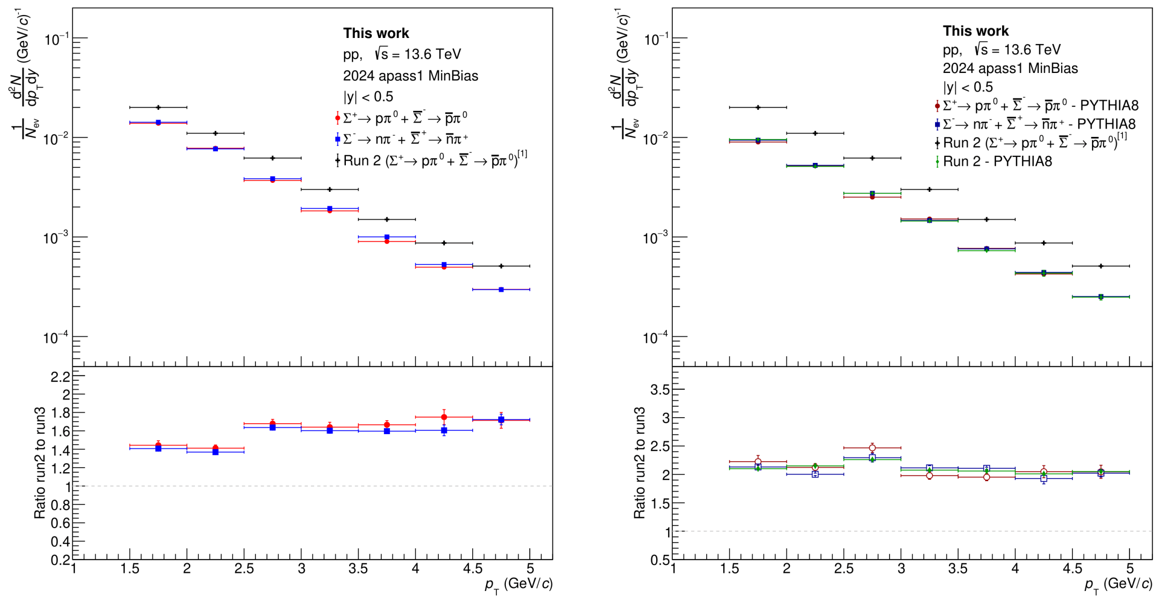

Fig. 10: In the left panel, comparison between $\Sigma^{\pm}$ yields obtained in this work (red and blue) and the Σ^{+} yield resulting from Run 2 analysis (black - data from [11]). In the right panel, comparison between PYTHIA 8 [10] MC generated yields (red and blue), Run 2 data (black) and Run 2 MC yields, generated using the same MC model PYTHIA 8 (green). In bottom panels, ratios to Run 2 data are shown.

8 Cross-check: Ξ^{-} production analysis

To check whether the discrepancy between the Run 3 and Run 2 data observed for the Σ yields is a systematic effect introduced by the reconstruction method, the analysis was repeated on the decay of a different particle. The Ξ^{-} decay into $\Lambda + \pi^{-}$ (with a branching ratio of B.R. $= (99.89 \pm 0.03)\%$ [4]) was chosen in this regard, as it is characterized by a very clean signal with high statistics, which can be easily isolated on the Armenteros-Podolanski plot (see the magenta half-ellipse in Fig. 1). Selection cuts applied to obtain the invariant mass distributions in this case are the same used to isolate the $\Sigma^{-} \rightarrow \mathrm{n} + \pi^{-}$ decay, except for those in the Armenteros-Podolanski variable $q_{\mathrm{T}}^{\mathrm{AP}}$, which is now required to lie within the [0.95, 1.45] interval.

8.1 Efficiency × acceptance

The reconstruction efficency × detector acceptance was computed from the MC data sample with the same procedure used for the Σ, and is shown as a function of both p_{T} and decay radius in Fig. 11. The values obtained are comparable with the ones for the $\Sigma^{-} \rightarrow \mathrm{n} + \pi^{-}$ channel, as it would be expected considering the similar decay topology and the lifetimes of the two mother particles, both of the order of ≈ 150 ps. In Fig. 11 the efficiency for $\overline{\Xi}^{+}$ is also reported, and no significant differences can be seen between the particle and antiparticle results.

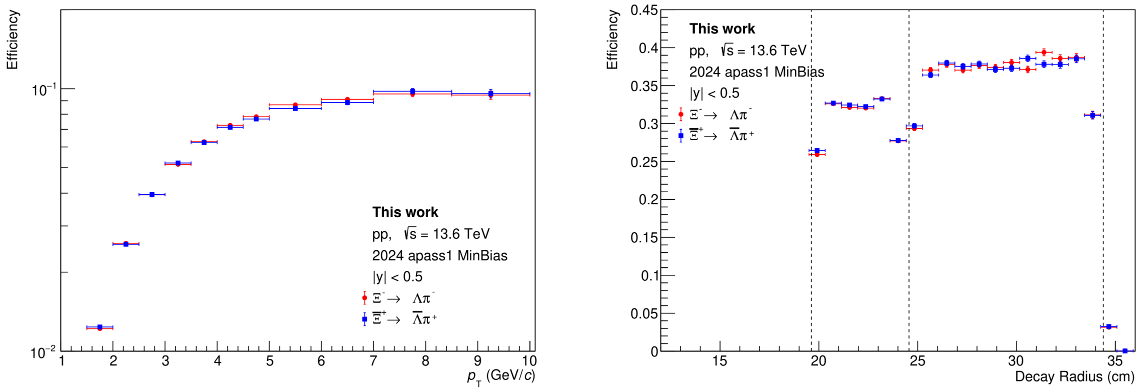

Fig. 11: Efficiency as a function of the transverse momentum (left) and of the reconstructed decay radius (right) of Ξ^- and $\overline{\Xi}^+$. In the right panel, the positions of the 4^{th}, 5^{th} and 6^{th} ITS layers are shown as vertical dashed lines. Error bars of the data points correspond to the statistical uncertainties.

8.2 Signal extraction

To extract raw spectra from invariant mass distributions, the combinatorial background template is first computed using the same rotational technique applied in the Σ analysis. The $\Xi^- + \overline{\Xi}^+$ signal is then modeled with a Crystal Ball distribution, with tail parameters fixed after a preliminary fit on the MC mass shape, convoluted with a Gaussian to keep track of resolution differences between data and MC. In this case, as it can be noticed from the plots in Fig. 12, the Armenteros-Podolanski cuts are not sufficient to completely eliminate the signal coming from $\Sigma \to \mathrm{n} + \pi$ decays, which then still appears as a wider peak on top of the combinatorial background of the $\Lambda + \pi$ invariant mass distribution. To account for this contamination, a third component modeled with a wide Gaussian distribution is added to the total fit. The raw counts of the signal for each p_{T} bin are extracted from the normalization factor of the Crystal Ball distribution obtained from the fit, computed over the [1.29, 1.36] GeV/c^2 interval.

8.3 Spectrum computation

Finally, the $\Xi^- + \overline{\Xi}^+$ p_{T}-differential yields corrected by the efficiency and normalized to the total number of events are computed using eq. 9. The shape obtained is shown in the left panel of Fig. 13: the spectrum was fitted with a Lévy-Tsallis function [9] with good results; from this fit the integrated rapidity density $\langle \mathrm{d}N/\mathrm{d}y \rangle$ for the $\Xi^- + \overline{\Xi}^+$ is estimated to be

$$\langle \frac{\mathrm{d}N}{\mathrm{d}y} \rangle (\Xi^- + \overline{\Xi}^+) = 0.0206 \pm 0.0003 \text{ (stat)}$$

This time, the differential yield was compared with that obtained from the same Run 3 data sample, but applying a more standard analysis method, based on the complete reconstruction of the charged products of Ξ^- decay cascades ($\Xi^- \to \Lambda + \pi^- \to \mathrm{p} + \pi^- + \pi^-$). This comparison is reported in the right panel of Fig. 13. A significant discrepancy between the two analyses is found in this case too, although its magnitude is lower than the one observed for Σ baryons: the values from this work are underestimated by a $15-20\%$ factor, which appears to increase to 35% in higher p_{T} intervals, where although the signal extraction procedure may become less reliable to the increasing fraction of Σ contaminants in the mass distributions (observe the bottom row plots in Fig. 12).

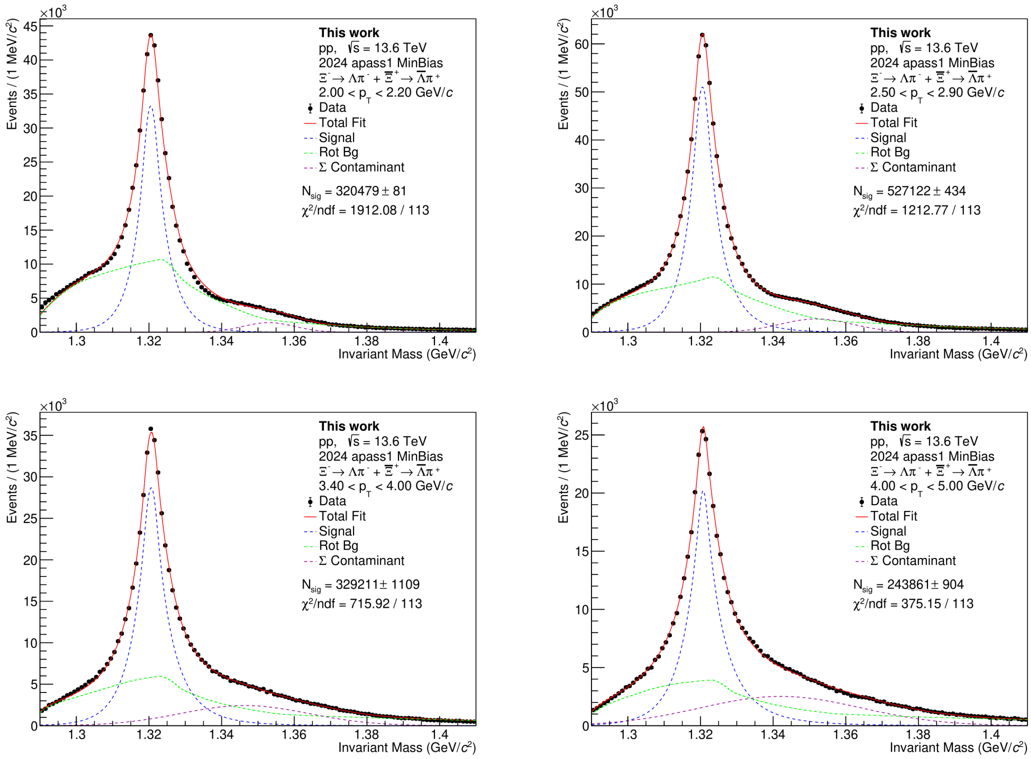

Fig. 12: Invariant-mass distributions of $\Xi^- + \overline{\Xi}^+$ for the $\Lambda(\overline{\Lambda}) + \pi^{\mp}$ decay in different p_{T} intervals. Error bars of the data points correspond to the statistical uncertainties. The Crystal Ball distribution for Ξ^- signal is shown in blue, the Gaussian curve added to account for Σ contamination in magenta. The rotational background template is the dashed green line, while the total fit function, sum of all component, is the red one.

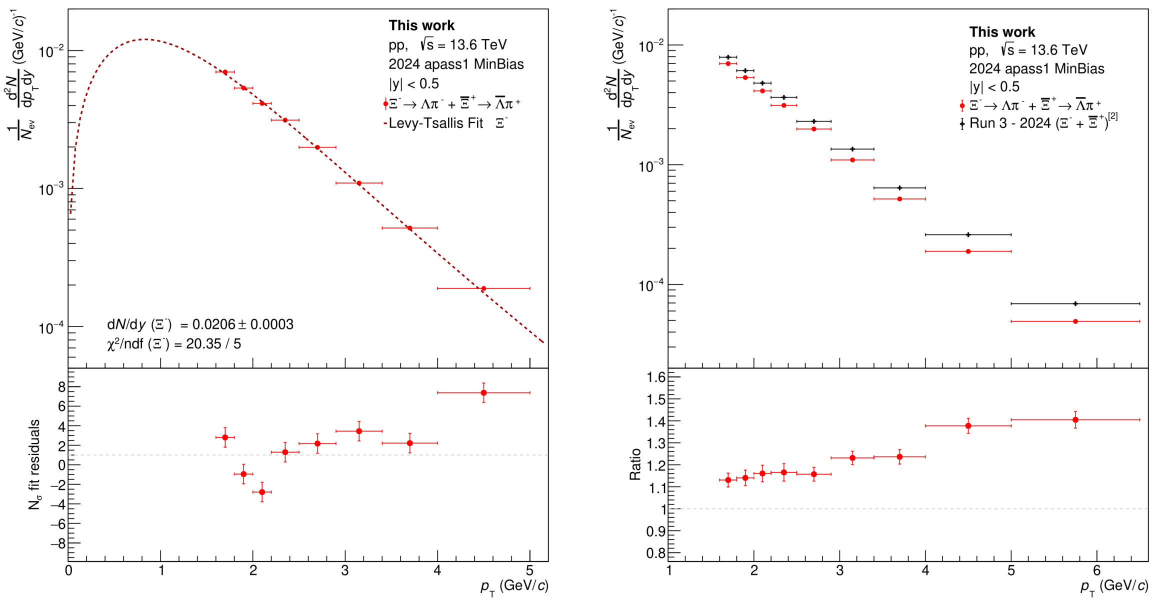

Fig. 13: In the left panel, corrected and normalized p_{T}-differential yield for $\Xi^- + \overline{\Xi}^+$, fitted with a Lévy-Tsallis function (fit residuals shown in the bottom panel). In the right panel, comparison between $\Xi^- + \overline{\Xi}^+$ yield with reference obtained from the same data sample, but applying standard cascade reconstruction methods for the analysis (in bottom panels, ratios to reference data are shown).

9 Summary and conclusions

In this work, the measurements of $\Sigma^- + \overline{\Sigma}^+$ and $\Sigma^+ + \overline{\Sigma}^-$ production yields in pp collisions at $\sqrt{s}$ = 13.6 TeV were presented. Thanks to the powerful tracking capabilities of the upgraded ITS detector installed at the ALICE experiment, an innovative analysis technique has been used to reconstruct the kink topology decays of the Σ baryons, allowing to isolate their signal with high purity and unprecedented efficiency, up to two orders of magnitude larger compared to previous approaches. In particular, the $\Sigma^- + \overline{\Sigma}^+$ production has been measured for the first time.

The differential yields as function of p_{T} are reported, as well as the integrated $\langle \mathrm{d}N/\mathrm{d}y \rangle$ values. Great compatibility is observed between the results obtained for Σ^+ and Σ^-. The experimental results are compared with the Monte Carlo event generator PYTHIA 8 and the Σ^+ production yields obtained from Run 2 data with a different analysis method. A systematic offset, constant across different p_{T} intervals, is observed between Run 2 and Run 3 results, with Run 2 data being approximately 60% larger than Run 3 ones. A significant discrepancy is also reported between MC generated yields and Run 2 data; however, no difference is seen among MC yields obtained using the techniques applied in this work or the ones used to process Run 2 data samples.

A Monte Carlo closure test was successfully performed to verify the reliability of the signal extraction procedure used to obtain raw spectra from invariant mass distributions.

As a last cross-check on the validity of the proposed analysis method, the production yield of an additional baryon, the Ξ^-, was also calculated. The extracted values were compared with the most recent results obtained with standard cascade reconstruction methods applied to the same Run 3 dataset. A better compatibility is found in this case, as values obtained in this work appear to be systematically underestimated only by a 15% factor.

However, in this analysis, no other discussion of systematic uncertainties has been carried out. A dedicated evaluation of systematic effects would represent a natural next step in order to consolidate the results. In particular, such a study could clarify the origin of the offset observed when comparing Run 2 and Run 3 data, and provide quantitative estimates of possible contributions from detector effects, background modeling, or signal extraction techniques.

Looking forward, the method developed and applied in this work opens the way to a large number of physics applications. As already outlined, precise measurements of Σ production will allow for detailed studies of strangeness enhancement, characterization of resonances such as the Λ(1405), and femtoscopic measurements of the Σ–p interaction. These applications show the potential impact of this analysis for both the understanding of the strong interaction and the physics of compact astrophysical objects such as neutron stars.

Acknowledgements

I would like to express my gratitude to my supervisors, for sharing their expertise with me, and for their guidance and constant support throughout every phase of this project. I am also thankful to the organizers of the Summer Student Programme, and to everyone who contributed to making my experience at CERN truly unforgettable.

References

[1] ALICE Collaboration, K. Aamodt *et al.*, "The ALICE experiment at the CERN LHC," *JINST* **3**, S08002 (2008).

[2] ALICE Collaboration, "Technical Design Report for the Upgrade of the ALICE Inner Tracking System," CERN-LHCC-2013-019, ALICE-TDR-020 (2013), https://inspirehep.net/literature/1305021.

[3] I. Ravasenga *et al.*, "Commissioning and Performance of the New ALICE Inner Tracking System in the First Phase of LHC Run 3," arXiv:2302.00432 [physics.ins-det] (2023).

[4] S. Navas *et al.* [Particle Data Group], "Review of particle physics," *Phys. Rev. D* **110**, no. 3, 030001 (2024), doi:10.1103/PhysRevD.110.030001.

[5] T. Hyodo, "What we know about the $\Lambda(1405)$," *AIP Conference Proceedings* **1735**, 020012 (2016), arXiv:1512.04708 [hep-ph].

[6] I. Vidana, V. Mantovani Sarti, J. Haidenbauer, D. L. Mihaylov, and L. Fabbietti, "Neutron Star Properties and Femtoscopic Constraints," arXiv:2412.12729 [nucl-th] (2025).

[7] J. Podolanski and R. Armenteros, "III. Analysis of V-events," *Philosophical Magazine Series 1* **45**, 13–30 (1954).

[8] T. Skwarnicki, "A study of the radiative cascade transitions between the Upsilon-Prime and Upsilon resonances," Ph.D. thesis, Institute of Nuclear Physics, Krakow, DESY F31-86-02 (1986), https://inspirehep.net/literature/230779.

[9] C. Tsallis, "Possible Generalization of Boltzmann-Gibbs Statistics," *J. Statist. Phys.* **52**, 479–487 (1988).

[10] P. Skands, S. Carrazza, and J. Rojo, "Tuning PYTHIA 8.1: the Monash 2013 Tune," *Eur. Phys. J. C* **74**, no. 8, 3024 (2014), arXiv:1404.5630 [hep-ph].

[11] ALICE Collaboration, S. Acharya *et al.*, "Σ^+ production in pp collisions at $\sqrt{s} = 13$ TeV," arXiv:2508.20808 [nucl-ex] (2025).